Contact Mechanics-based Gait Generation and Trajectory Tracking Algorithm for Radial-skeleton Robots

Dun Yang[a,*], Yunfei Liu[a,*], Fei Ding[a], Kangxin Hu[a], Yang Yu[a,**]

[a]*School of Aeronautic Science and Engineering, Beihang University, Beijing 100191, China*

Abstract

Radial-skeleton shape-changing robots are rough-terrain robots and exhibit many advantages in the aspect of mobility, such as excellent terrain adaptability, light weight, good portability, and stable configuration. However, existing gait generation methods are rough and yield low tracking accuracy because the leg-ground contact friction is difficult to predict and control. In addition, no closed-loop control scheme has been proposed for this type of robot. In this study, we designed a 12-legged radial-skeleton robot with a radial expansion ratio of 2.08. Based on the prototype, we proposed a high-precision gait generation algorithm that can be used to any multi-legged radial-skeleton robot and implemented a closed-loop control scheme for accurate path tracking. Combining the contact friction and multi-body dynamics model, the robot prototype exhibits the advantages of omnidirectional motion, high-precision tracking, and motion robustness. By manufacturing a prototype and conducting comparative experiments, we verified that the proposed method yields good performance in terms of trajectory tracking accuracy and robustness in the cases of unknown terrain and interference.

Keywords: Radial-skeleton Robot, Gait Generation, Contact Mechanics, Locomotion, Complex Terrain

1. Introduction

The existing wheeled and legged robots (Lee et al., 2020; Li et al., 2021; Yang et al., 2020) are not suitable for ground detection tasks in extreme terrains, such as cave inspection (Dubowsky et al., 2008), planetary surface exploration (Antol, 2005), jungle demining (Tilden, 1995), and ruins exploration (Takemori et al., 2018), because traditional mobile robots have fixed body structures, which make it difficult to maintain stability (Xian & Yongchun, 2020). Moreover, they

*Co-first author

**Corresponding author

Email addresses: dunyang@buaa.edu.cn (Dun Yang), yu.yang@buaa.edu.cn (Yang Yu)

cannot perform an omnidirectional movement, which means that once they fall, it is difficult to get them upright in a complex environment. In this paper, we proposed shape-changing mobile robots with redundant degrees of freedom, symmetrical structure, and simple movement mode as promising solutions for the aforementioned complex terrain exploration tasks. The ability to adjust the contact surface ensures that these robots can adapt to complex terrain, scale-variable crevices, and confined space. According to the structural features, three-dimensional (3D) shape-changing robots can be categorized into three types:

(1) Edge-skeleton shape-changing robots: The edges are composed of actuators or links, forming the robot skeleton to make space for the payload. According to the type of edges, edge-skeleton shape-changing robots can be classified as rigid-shell robots (Bicchi et al., 1997; Hirano et al., 2013; Joshi et al., 2010; Mojabi et al., 2002; Mukherjee et al., 2002; Otani et al., 2006), soft-shell robots (Masuda & Ishikawa, 2017; Sugiyama & Hirai, 2006; Wait et al., 2010), and multi-linkage robots (Abrahantes et al., 2007; Hamlin & Sanderson, 1994; Liu et al., 2012; Sastra et al., 2009; Wang et al., 2016; Yamawaki et al., 2003; Yim, 1994; Yim et al., 2000). Zagal et al. (2012) proposed an octahedral rigid-edge-skeleton robot by using a hydraulic drive; The structural deformability and high symmetry enable the robot to pass through narrow L-shaped, T-shaped, and Y-shaped pipe joints without a steering mechanism. Sugiyama & Hirai (2006) used three circular elastic rings to construct a spherical robot that can be driven by shape memory alloy wires. The rolling motion is achieved by using the COG offset method to deform its shape and achieved rolling motion by using the COG offset method to deform its shape. Wei et al. (2019) proposed a multi-link robot comprising six node modules and 12 planar RRR chain modules that can switch between multiple rolling directions. The main advantages of these types of robots are their high deformation ratio, which yields reconfigurability and strong adaptability on complex terrains. However, configuration planning in advance requires a large amount of effort, and contact mechanics is difficult to model and describe, resulting in insufficient control accuracy.

(2) Tensegrity robots: Tensegrity structure is a stable spatial structure with self-stress balance and is realized by connecting compression members and flexible tension cables. Tensegrity structure offers the advantages of light weight, foldability, and good environmental adaptability (Wang et al., 2022). According to the imitation object and shape, tensegrity robots can be classified as prismatic tensegrity robots (Bingyu et al., 2020), spherical tensegrity robots (Baines et al., 2020; Mintchev et al., 2018; Shibata & Hirai, 2010; Vespignani et al., 2018), humanoid musculoskeletal tensegrity robots (Hong & Choi, 2019; Jung et al., 2019; Lessard et al., 2016; Sun et al., 2019), and bionic tensegrity robots (Abourachid et al., 2019; Hustig-Schultz et al., 2017; Mirletz et al., 2014; Shintake et al., 2020). Wang et al. (2022) studied quadrangular robots and realized steerable rolling motion by using the structural deformation of FPTR. NASA launched the superball project for space exploration and designed a low-cost, modular, rapid prototyping tensegrity robot to provide a medium for future development (Vespignani et al., 2018). Lessard designed a modular humanoid

tensegrity manipulator that functions similarly to human elbows and shoulders (Lessard et al., 2016). The complex dynamics of tensegrity robots make it challenging to control their movement. No fully autonomous tensegrity robot has been developed that can navigate in unstructured terrains. Traditional control methods do not consider self-collision or environmental contact dynamics, thus limiting their applicability in real-world applications. Analytical control methods are not employed in hardware experiments because they rely on accurate state information which is difficult to obtain (Shah et al.).

(3) Radial-skeleton robots: Radial-skeleton robots (Gheorghe et al., 2010; Mateos, 2020; Nozaki et al., 2018, 2017; Wagenknecht & Apostolopoulos, 2010; Wilson et al., 2008) are bio-inspired robots (inspired by sea urchins and tumbleweeds) with multi-radial legs and spherical structures. NASA proposed a tumbleweed-like planetary probe (Wilson et al., 2008) that can be driven by Martian wind to realize exploration; however, it lacks autonomous control capability. Inspired by sea urchins, Gheorghe et al. (2010) proposed a spherical robot that employs the telescopic mechanism to drive the robot. Researchers at CMU designed a 5-legged pneumatic planar robot prototype (Luders et al., 2008) and a spherical 12-legged pneumatic robot (Wagenknecht & Apostolopoulos, 2010). Researchers at the University of Tokyo in Japan developed a spherical robot (Nozaki et al., 2018, 2017) with 32 retractable legs to realize the continuous trajectory motion of straight line and curve based on the kinematics method. Researchers at MIT designed a high-expansion-ratio brake (Mateos, 2020). Compared with other two types of shape-changing robots, radial-skeleton robots have low deformation ability and flexibility but are more controllable and predictable.

However, the existing motion control method employed in radial-skeleton robots does not leverage the advantages of high controllability and predictability of radial-skeleton robots, leading to oversimplified and incomplete gait planning and control frame. Manual designing does not enable taking full advantage of omnidirectional motion and is highly complex (Wagenknecht & Apostolopoulos, 2010). The straight-line motion scheme (Nozaki et al., 2018) based on inverse kinematics planning far exceeded the expected distance in the actual test because the rear-extended support leg pushes the front support leg forward during the rolling process. Zhang et al. (2021) proposed a method based on physics-driven locomotion planning by using an artificial dynamic model that can generate gait sequences in complex terrains. However, it is based on numerous assumptions and is thus far away from reality, and real-time control cannot be achieved. Some learning-based methods (Yang et al., 2022) are suitable in some scenarios. however, the gap between simulation results and real-world test results is too large. One main challenge for the above problem is to predict and control the relative sliding between the legs and the contact surface. Furthermore, the high-precision omnidirectional closed-loop gait control schemes have not been developed to date.

In this paper, we proposed a gait control framework by considering contact mechanics to enable multi-legged radial-skeleton robots to perform real-time omnidirectional gait planning in any posture and realize high-precision trajectory

tracking control. In addition, we designed a 12-legged radial-skeleton robot with a high expansion ratio to validate the performance. Moreover, we performed an open-loop gait accuracy comparison experiment and a closed-loop control experiment to demonstrate the advantages of high accuracy and robustness of the proposed method. The proposed method can serve as a unified control framework for radial-skeleton robots.

The contributions of this study are as follows:

- We proposed a high-precision gait control algorithm for the arbitrary multi-legged radial-skeleton robot by considering contact friction in gait generation. The robot can perform omnidirectional motion from any initial posture.
- We designed and manufactured a 12-legged radial-skeleton robot with a high telescopic ratio and established a dynamic model to analyze and simulate motion.
- We constructed an experimental system, systematically compared the advantages and disadvantages of the existing radial-skeleton robot gait generation algorithms, and verified the advantages of high precision and robustness offered by the proposed method.

The paper is organized as follows. In Section 2, the mechanical structure is outlined. In Section 3, the dynamics model and control frame are presented. In Section 4, the experimental and comparison results are presented. Finally, the conclusion and future work are discussed in Section 5.

2. Radial-Skeleton Robot Structure Design

2.1. Telescopic mechanism and body design

In radial-legged robots, the high extension ratio mechanism is a vital part of the robot's deformation ability and influences the shape-changing ability and motion. When designing the telescopic mechanism, the requirements of a high elongation ratio, low complexity, large output, and low weight must be considered. The high extension ratio telescopic mechanism designed in this study adopts the two-way pulley mechanism, which is widely used in multi-section elevators.

In the proposed design, the telescopic mechanism, as seen in Fig.1-a, is driven by an electric cylinder fixed on the robot base. A lightweight aluminum slide rail is used to increase the extension ratio. An electric cylinder and a putter constitute the linear actuator. The slide plate, rail seat, and pulley compose the slide rail. Coil-cylinder connectors, coil-plate connectors, and putter-seat connectors are fabricated using 3D printing and are used to constrain movement. When the liner actuator starts moving, the electric cylinder is fixed, and the pulley, rail seat, and connector begin telescoping along with the putter. With the constraints of a fixed coil-cylinder connector and coil-plate connector, the slide plate moves under the drive of the putter.

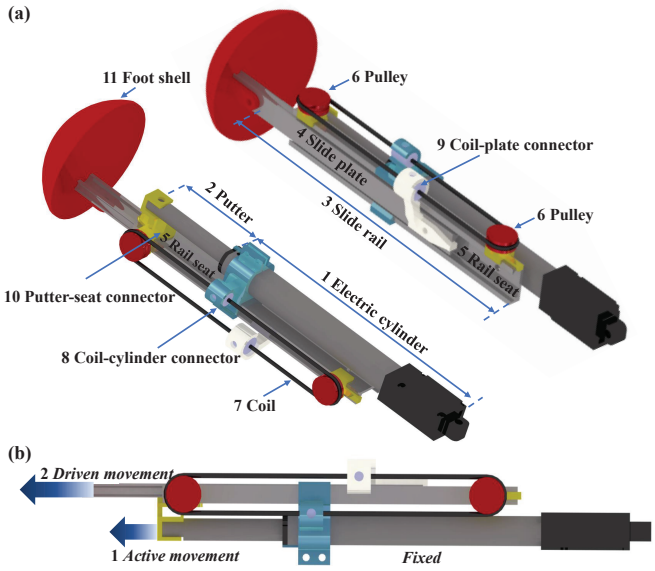

Fig. 1. (a) Telescopic leg and components (b) Diagram of expansion principle

Table 1: Parameters of extension mechanism

Parameter	Value
Extension ratio	2.08
Max length	384.121mm
Minimum length	184.121mm
Actuator extension speed	2.8cm/s
Max force	25N
Back drive force	25N
Overall weight	144.2g

The proposed mechanism can be explained using the principle of motion synthesis, as seen in Fig.1-b. Taking the first section as the research object. The pulley fixed on the first section moves with the second section at a speed of V. A point on the other side of the coil is fixed on the robot base at a relative speed to the first section, while the coil on the other side moves to the left. The relative speed of the second section is $Ve = V$, and the second section extends at the speed of $2V$. Thus, the extension ratio of the telescopic mechanism is increased. Details regarding the telescopic mechanism performance are presented in Table.1.

For deciding the number of telescopic legs when designing the robot body, many factors must be considered, such as the weight, deformation capacity, and design difficulty. Increasing the number of telescopic legs improves the robot's deformation ability but increases the weight of the robot and the size of the central connector. As shown in Fig.2, we arranged 12 telescopic legs on the

central vertical line of the dodecahedron's central, achieving a trade-off between design difficulty and deformation ability. The symmetrical distribution of legs yields the advantages of omnidirectional movement and all-posture movement ability.

The central base connects multiple telescopic mechanisms In the form of sleeve and bolt combinations. To improve the extension ratio, the radial size of the non-extensible parts, such as the base, should be as small as possible. After assembly, the extension ratio of the whole robot does not decrease much relative to that of a single telescopic mechanism. The center base is hollowed out to reduce the weight, and a small IMU(Inertial Measurement Unit) is installed to measure nine physical quantities in real-time, including the angle, angular velocity, and acceleration in all three directions. Electric cylinders bear axial forces in industrial applications, and the bearing capacity for vertical forces is poor. When the robot moves, the foot is subjected to vertical forces. The connection between the motor and the cylinder is the most vulnerable part of the robot and might bend during movement. Therefore, we designed a sleeve and a connecting bracket for the connection to increase the structural strength and reduce deformation. The robot parameters are presented in Table.2.

Table 2: Parameters of the robot

Parameter	Value
Extension ratio	1.97
Max diameter	811.84mm
Minimum diameter	411.84mm
Overweight	1819.6g

2.2. Control system

To realize closed-loop control, the robot control system can be divided into three parts, as shown in Fig.3: perception, calculation, and motor execution. The IMU measures the angle, angular velocity, and acceleration in real time and

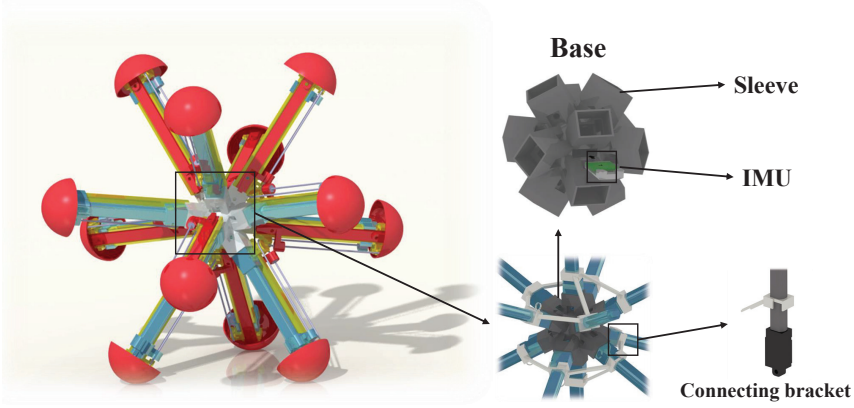

Fig. 2. Robot and components design.

transmits the data to the microcontroller through serial-port communication. The Arduino microcontroller, responsible for the calculation function, converts the sensor's original information into the robot's posture and determines each leg's moving speed and direction. Finally, the telescopic foot movement information is transmitted to the motor governor, which controls the DC motor in the electric cylinder to execute the command. The control system employed in this paper uses a 5-V power supply to power the MCU(Microcontroller Unit) and IMU and a 12-V power supply to power the motor governor and motor.

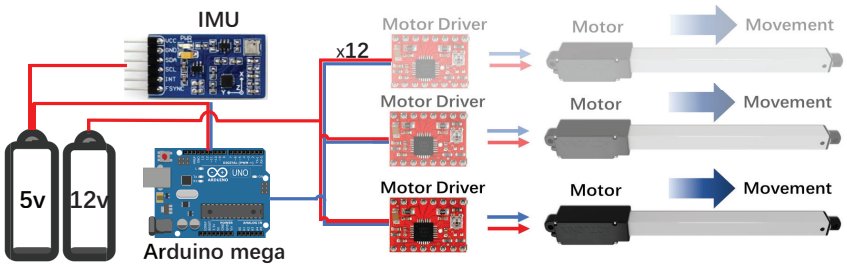

Fig. 3. Diagram of control system

3. Dynamic Model and Control Frame

Radial-skeleton robots mainly move by performing the rolling motion, which means that the center of gravity moves out of the support triangle when the legs are expanded. During the expansion and contraction of the legs, the friction between the leg end and the ground greatly affects the robot's motion accuracy. The rolling process may also cause hits between the leg-end and the ground, resulting in uncertainty and damage to the structure. Therefore, the high-precision dynamic model considering friction contact is of great significance in the research on robot motion control, especially in simulation studies and the transformation from simulation to reality.

3.1. Dynamic model and contact force calculation

A single rigid body is used to describe the radial-skeleton robot because the robot's mass is concentrated at the base. Experiments in Section 4 have demonstrated that the accuracy of this simplified model is sufficient in the case of relatively slow movement. The state variables of the robot can be described as follows:

$$\boldsymbol{q} = [x, y, z, \lambda_0, \lambda_1, \lambda_2, \lambda_3, v_x, v_y, v_z, \omega_x, \omega_y, \omega_z]^{\mathrm{T}} \tag{1}$$

where $[x, y, z]$ and $[\lambda_0, \lambda_1, \lambda_2, \lambda_3]$ represent the centroid position in the inertial frame and quaternions in body-fixed coordinate, respectively, and $[v_x, v_y, v_z]$ and $[\omega_x, \omega_y, \omega_z]$ represent the centroid velocity in the inertial frame and the angular

velocity in the body axes, respectively. These state variables hold the following dynamic relationships, which are deducted using the Newton equation:

$$[\dot{x}, \dot{y}, \dot{z}, \dot{v}_x, \dot{v}_y, \dot{v}_z]^{\mathrm{T}} = \left[v_x, v_y, v_z, \frac{F_x}{m}, \frac{F_y}{m}, \frac{F_z}{m}\right]^{\mathrm{T}} \tag{2}$$

where m is the weight of the robot, and $[F_x, F_y, F_z]^{\mathrm{T}}$ is the force vector acting on the center of mass, including contact forces and gravity forces. Taking the derivative of the quaternion, we obtain

$$\left[\dot{\lambda}_0, \dot{\lambda}_1, \dot{\lambda}_2, \dot{\lambda}_3\right]^{\mathrm{T}} = \frac{1}{2}\begin{bmatrix} -\lambda_1 & -\lambda_2 & -\lambda_3 \\ \lambda_0 & -\lambda_3 & \lambda_2 \\ \lambda_3 & \lambda_0 & -\lambda_1 \\ -\lambda_2 & \lambda_1 & \lambda_0 \end{bmatrix}\begin{bmatrix} \omega_x \\ \omega_y \\ \omega_z \end{bmatrix} \tag{3}$$

By using the Euler equation to obtain the derivation of the angular velocity, and selecting the inertial spindle coordinate system as the body axes, we obtain

$$\begin{cases} J_x\dot{\omega}_x + (J_z - J_y)\,\omega_y\omega_z = M_x^{\tau} \\ J_y\dot{\omega}_y + (J_x - J_z)\,\omega_z\omega_x = M_y^{\tau} \\ J_z\dot{\omega}_z + (J_y - J_x)\,\omega_x\omega_y = M_z^{\tau} \end{cases} \tag{4}$$

where J is the inertia tensor, and M is the external moment in the body axes. Because J is equal in all three dimensions, Eq. (4) can be simplified as the following:

$$[\dot{\omega}_x, \dot{\omega}_y, \dot{\omega}_z] = \left[\frac{M_x^{\tau}}{J_x}, \frac{M_y^{\tau}}{J_y}, \frac{M_z^{\tau}}{J_z}\right] \tag{5}$$

Combining Eqs. (2), (3), and (5), we obtain the dynamics equation of the robot system.

Next, the contact force is calculated. Previous studies on radial-skeleton robots have ignored the influence of contact mechanics, resulting in the great disparity in gait deployment between simulation and reality in the case of open-loop control. When the field robot moves in a real environment, it witnesses complex contact, collision, sliding, and separation behaviors with different types of terrain. We used the soft sphere discrete element method (Crowe et al., 1998) used in discrete dynamics to describe the interaction between the leg-end and the ground because this method has wider adaptability and higher accuracy for different contact conditions by using the relative deformation degree between the contact objects.

The single-leg embedment depth of the spherical shell is considered , as shown in Fig.4:

$$\delta_N = |\boldsymbol{r}_l + \boldsymbol{r}_s - \boldsymbol{r}_g| \tag{6}$$

where $\boldsymbol{r}_l$ is the leg-end shell center vector in the inertial coordinate system.

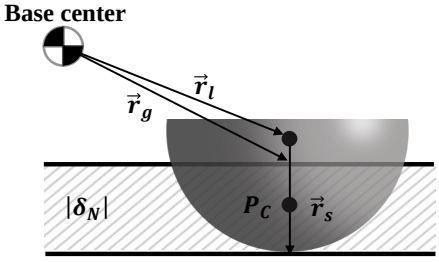

Fig. 4. Soft sphere contact model.

When the spherical shell (with radius $\boldsymbol{r}_s$ and position $\boldsymbol{r}_l$) and the ground (with position $\boldsymbol{r}_g$) come in contact, the degree of deformation caused by normal extrusion can be expressed by the amount of overlap δ_N. The normal elastic restoring force produced by extrusion deformation can be expressed using Hooke's law of linear elasticity:

$$\mathrm{F}_{N,\text{ elastic}} = k_N \delta_N \overrightarrow{\boldsymbol{n}} \tag{7}$$

where, unit normal vector $\overrightarrow{\boldsymbol{n}} = (\boldsymbol{r}_g - \boldsymbol{r}_l) / |\boldsymbol{r}_g - \boldsymbol{r}_l|$, and k_N is the normal elastic coefficient, which reflects the stiffness of granular materials. Because the contact is not an ideal elastic contact, viscous dissipation force is observed due to particle viscoelasticity and normal relative motion.

$$\mathbf{F}_{N,\text{ damping}} = C_N \mathbf{u}_N \tag{8}$$

where C_N is the normal damping coefficient. The normal relative velocity of two particles at the contact point can be expressed as

$$\mathbf{u}_N = \left[(-\mathbf{v}_p) \cdot \overrightarrow{\boldsymbol{n}}\right] \overrightarrow{\boldsymbol{n}} \tag{9}$$

where $\mathbf{v}_p$ is the linear velocity of the contact point P_c, which is defined as the center of embedment depth along the spherical shell radius, as seen in Fig.4. $\mathbf{v}_p$ can be calculated as follows:

$$\mathbf{v}_p = \mathbf{v}_{\text{base}} + \mathbf{w}_{\text{base}} \times \mathbf{r}_p + \mathbf{v}_{\text{expend}} \tag{10}$$

where $\mathbf{v}_{\text{base}}$ and $\mathbf{w}_{\text{base}}$ are the velocity and angular velocity of the base, respectively, and $\mathbf{v}_{\text{expend}}$ is the leg's radial expansion speed. Combining Eqs. (7) and (8), the normal contact force at the contact point can be expressed as

$$\mathbf{F}_N = k_N \delta_N \overrightarrow{\boldsymbol{n}} + C_N \mathbf{u}_N \tag{11}$$

The mechanical properties of the normal contact force are mainly controlled by the elastic coefficient k_N and damping coefficient C_N, which can reflect the strength characteristics and energy dissipation capacity of spherical shell materials, respectively, under external pressure. In the experiment, we selected

these coefficients by comparing the simulation and prototype experimental results. The prototype contacts the rigid ground with a large elastic coefficient k_N. When applying this value of k_N into the simulation, a very small simulation step size must be used to avoid excessive contact force. To achieve a trade-off between the calculation duration and simulation accuracy, we adopt adopted a relatively low elastic coefficient k_N and a large step size.

When considering the tangential contact force, the tangential relative motion between the spherical shell and the ground must be analyzed. The surface microstructures of the shell and the ground squeeze in the vertical direction of $\vec{n}$, resulting in deformation that can be described by the tangential contact deformation vector:

$$\boldsymbol{\delta}_S = \int_{t_0}^{t} \boldsymbol{u}_S(\tau) d\tau + \boldsymbol{\delta}_{S0} \tag{12}$$

where $\boldsymbol{\delta}_{S0}$ is the tangential contact deformation vector at time t_0 (if time t_0 is the initial contact time, $\boldsymbol{\delta}_{S0} = 0$). The tangential relative velocity at the contact point can be expressed as

$$u_{\mathrm{S}} = \mathbf{v_p} - \mathbf{u}_{\mathrm{N}} \tag{13}$$

Similar to the normal contact model, the tangential stiffness coefficient k_S is introduced, and the tangential elastic restoring force generated by tangential extrusion deformation can be expressed as:

$$\mathrm{F}_{\mathrm{S,\ elastic}} = k_S \delta_S \tag{14}$$

Tangential relative motion can also produce tangential viscous dissipation force:

$$\mathbf{F}_{S,\ \mathrm{damping}} = C_S \mathbf{u}_S \tag{15}$$

Limited by contact surface shear strength, when $\mathbf{F}_{S,\ \mathrm{damping}}$ reaches a certain value, a plastic slip occurs on the contact surface of particles. The corresponding slip conditions can be expressed using the Coulomb friction coefficient μ_S and the amplitude of normal contact force F_N at the contact surface of the granular material. Thus, the complete tangential contact force model can be expressed as:

$$\mathbf{F}_S = \begin{cases} k_S \boldsymbol{\delta}_S + C_S \mathbf{u}_S, & |k_S \boldsymbol{\delta}_S| < \mu_S F_N \\ \mu_S F_N \boldsymbol{\delta}_S / |\boldsymbol{\delta}_S|, & |k_S \boldsymbol{\delta}_S| \geq \mu_S F_N \end{cases} \tag{16}$$

where k_S is the tangential stiffness coefficient, C_S is the damping coefficient, and μ_S is the tangential friction coefficient and is adopted as the empirical coefficient.

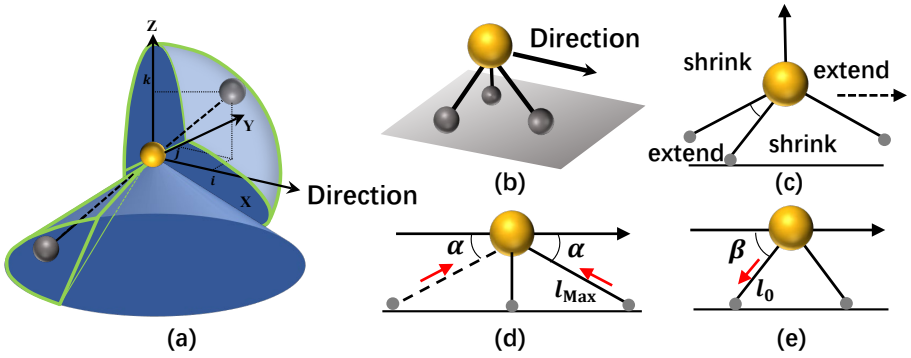

Fig. 5. Gait generation approach

3.2. Omnidirectional gait planning

Leg motion planning is performed as follows. To simplify the planning by using robot symmetry property, the leg speed must be selected according to the leg's spatial position relative to the forward direction. First, the leg's spatial position should be determined, as shown in Fig.5-a, to establish the forward direction coordinate system. The coordinate origin is the robot base, the x-axis is parallel to the forward direction at the current time, and the z-axis is vertically upward; thus, the right-hand coordinate system is established. The spatial position can be determined by calculating the direction vector of the leg in this coordinate system:

$$\overrightarrow{r_l} = (\boldsymbol{i}, \boldsymbol{j}, \boldsymbol{k}) \tag{17}$$

Finally, the vector value is inputted into the function 18 to calculate the control quantity v_{i}:

$$v_i = v\left(\vec{r}_i\right) \tag{18}$$

where $\vec{r}_i$ is the unit direction vector of leg_i, and v_{i} is the motion command of leg_i, that is, the moving speed of the telescopic leg.

The design of the leg control function v_i must meet many requirements. First, the leg must have omnidirectional movement capability under any initial posture. Second, the trajectory achieved using this design method should be as stable as possible to reduce error in the trajectory tracking process. Considering the disadvantage that the prototype cannot sense the leg length, it is necessary to control the leg length in the state of the maximum or minimum value in a movement to avoid the accumulated error caused by calculating the telescopic foot length by integrating the telescopic foot speed. Moreover, the leg control function must have a relatively simple form for improving the operation speed in real-time control.

In short, we hope that in the forward direction, with the robot base as the center, the front suspended leg can extend in motion to move forward, and the rear landing legs can extend to support the robot rolling. The other feet should shrink as far as possible to adjust the mass distribution. This telescopic area needs to be defined through the critical state. Considering two critical moving robot states, the vector space of the leg's direction is divided into four parts to realize the velocity planning of all the legs, as shown in Fig.5-c.

In the Fig.5, l_0 and $l_{\max}$ are the shortest and largest length of the leg, respectively ($l_{\max}$=1.97l_0), and α and β are the critical state angles formed by the landing legs and the horizontal plane.

The first critical state determines when the front legs begin to shorten, as shown in Fig.5-d. At this moment, suppose that we have three landing legs: two legs are in the shortest state, positioned vertical to the ground, and the front leg is in the longest state. The angle between the longest leg and the horizontal plane is the boundary value when the leg starts to come in contact with the ground. To make the movement as smooth as possible, the front leg should begin to shrink at this angle. A small angle α will cause unstable rolling movement and heavy impact, and a large angle α will cause movement obstruction. Due to the symmetry, the rear legs should also stop further elongation at angle α . The exact value of α is determined experimentally.

The second critical state determines when the rear legs begin to extend, as shown in Fig.5-e. When the three landing legs are in the shortest state, the angle between the plane formed by the two rear legs and the horizontal plane is the boundary angle β, which has a value of $60° - 90°$. In prototype experiments, we found that β influences the accuracy of the trajectory. We adopted the appropriate value through experiments.

Except for these aforementioned leg spaces, the control command of other legs is performed according to the law that the front legs extend and the rear legs shrink, resulting in an efficient centroid configuration. The control laws can be expressed as follows:

$$\begin{cases} v_{\mathrm{i}} = -v & k < 0, i^2 + j^2 < \cos^2(\alpha), i > -\cos(\boldsymbol{\beta}) \\ v_{\mathrm{i}} = v & k < 0, i^2 + j^2 < \cos^2(\alpha), i \leq -\cos(\beta) \\ v_{\mathrm{i}} = -v & \left\{k < 0, i^2 + j^2 \geq \cos^2(\alpha), i < 0\right\} \cup \{k > 0, i < 0\} \\ v_{\mathrm{i}} = v & \left\{k < 0, i^2 + j^2 \geq \cos^2(\alpha), i > 0\right\} \cup \{k > 0, i > 0\} \end{cases} \tag{19}$$

Finally, a relatively simple form v_i can be obtained. The direction vector space of the legs is divided into four regions, as shown in Fig.5-c, where v is the maximum leg speed, and the extension is taken as the positive direction.

In the prototype experiment, the unit direction vector of each leg in the fixed coordinate system was determined by the configuration of the legs, and the IMU sensor provided the posture data of the base. According to the robot posture and forward direction information, the unit direction vector of each leg in the control vector coordinate system was obtained by the coordinate transformation in the microcontroller. Then, the microcontroller determined the control command of each leg and sent the signal to the actuator.

3.3. Trajectory tracking

During tracking in a specific desired path, the traditional robot, like wheeled robots, needs to consider the limits of the turning radius and take a series of actions to adjust its posture, such as backward movement and reversing. However, in radial-skeleton robots, the symmetrical structure enables omnidirec-

tional movement, and the overall motion planning of the robot is not affected by the posture.

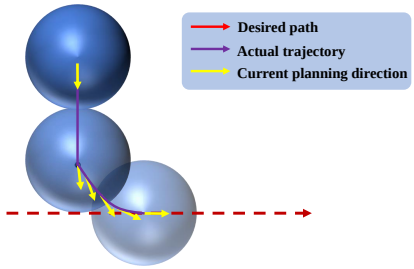

Fig. 6. Trajectory tracking approach

Experimental results revealed that the radial-skeleton robot prototype designed in this paper can turn in situ, change the direction of motion, and turn simultaneously when the forward direction command changes. Therefore, in flat trajectory tasks, designed turning and other actions are not required, as demonstrated experimentally (Section 4.1). We adopted a simple circle drawing planning scheme to perform direction planning. As can be seen in Fig.6 , when the distance between the robot center and the desired path exceeded the robot radius, the planning direction of the robot was vertical to the desired path.

3.4. Movement control framework

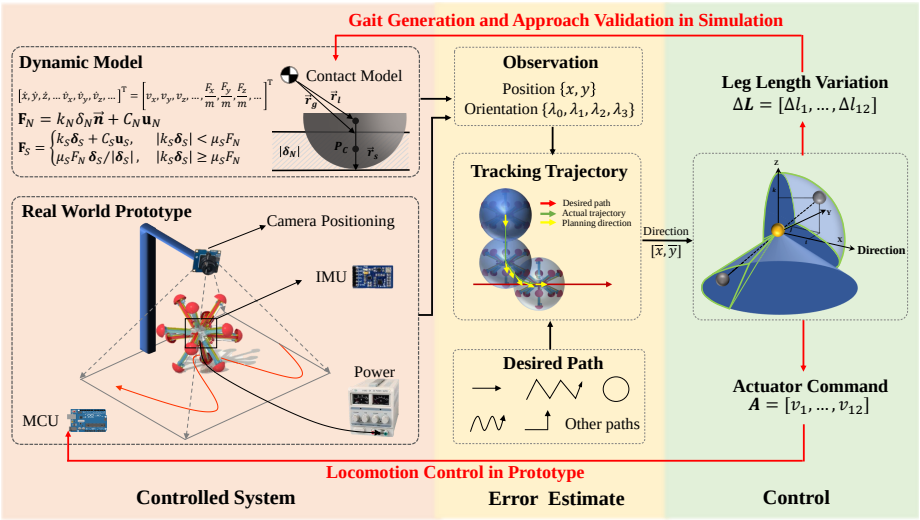

Fig. 7. Gait generation algorithm and movement control framework

We used the three aforementioned parts to realize two types of robot movement. The first type is virtual gait generation for open-loop deployment and

control method evaluation, and the second type is movement control for the closed-loop prototype, as shown in Fig.7.

First, we used the dynamic model to generate the gait sequence $\{L_{t_0}, L_{t_1}, \ldots, L_{t_n}\}$ in the simulation. Because contact mechanics was considered, we were able to simulate the real leg-ground contact behavior much more accurately and obtain the most appropriate simulation model parameters for prototype experiments.The contact model provides contact forces, $\mathbf{F}_N$ and $\mathbf{F}_S$, for single-body dynamic model to calculate the position $\{x, y\}$ and orientation $\{\lambda_0, \lambda_1, \lambda_2, \lambda_3\}$. By using the trajectory tracking algorithm, the next-step forward direction $[\bar{x}, \bar{y}]$ can be inferred using the observed states and the desired path. According to this direction, the action of each leg $\Delta \boldsymbol{L} = [\Delta l_1, \ldots, \Delta l_{12}]$ can be planned. The experimental results demonstrated that compared with other methods, the proposed method can predict the slipping of the leg on the ground and perform new gait planning, which cannot be realized by other open-loop gait generation methods; this makes the proposed open-loop deployment more accurate.

Second, we proposed the real-world prototype control frame for radial skeleton robots. The difference between it and the first usage is mainly in the controlled system, as shown in Fig.7. In real-world applications, the position and orientation of a robot are measured using the IMU and cameras. The error estimate and control stages are the same as in the former case. Finally, the actuators command, $\boldsymbol{A} = [v_1, \ldots, v_{12}]$, is calculated and recorded into an SCM(Single Chip Micyoco) system,and the robot begins to walk.

4. Experiments

To evaluate the movement performance of the proposed robot mechanism design, gait generation accuracy and closed-loop control accuracy, we performed movement demonstration experiments, gait accuracy comparison experiments with other algorithms and tracking accuracy and robustness test on the proposed motion control method.

4.1. Movement performance experiments

We performed movement performance experiments to qualitatively verify and demonstrate the performance of the prototype and the proposed method in the real world. Omnidirectional motion capability and complex motion demonstration were employed as the evaluation metrics.

Omnidirectional movement experiments: We set the robot to walk along eight uniform angles at the same initial position to validate the omnidirectional movement ability and track an L-shaped trajectory to verify the right-angle turning capability. All the experiments were based on gait generation in simulation and gait sequence open-loop deployment. Experimental results are shown in Fig.8. The red trajectory is the desired trajectory, and the blue dotted curve is the actual trajectory. The results revealed that the initial trajectory error in some specific directions was large in the omnidirectional movement experiments. However, it tracked the desired trajectory soon in the following

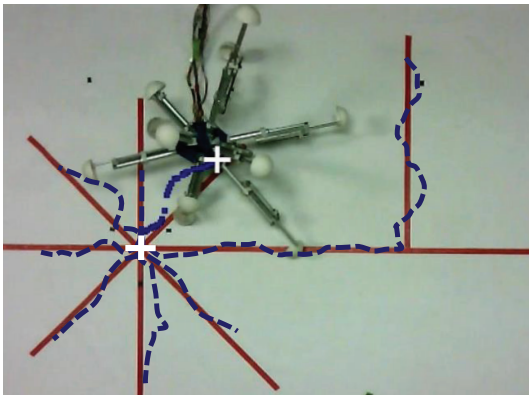

Fig. 8. Omni-direction experiments

steps. The tracking error for the L-shaped trajectory was larger in the latter half because the accuracy of the open-loop deployment was limited over such a long distance, and there were dead points caused by structural characteristics, resulting in movement direction uncertainty.

Comprehensive experiment: This experiment was performed to demonstrate the robot's movement advantage in a comprehensive task such as obstacle avoidance. As can be seen in Fig.9, when the robot moved along the red desired trajectory, an obstacle was suddenly introduced. The robot first switched directions at an obtuse angle, intersecting with the desired trajectory direction, and then switched directions at right angles and followed acute angles along the obstacle, and finally continued to track the given trajectory. This experiment demonstrated that the fully symmetrical structure provides the advantages of obstacle avoidance and omnidirectional movement ability.

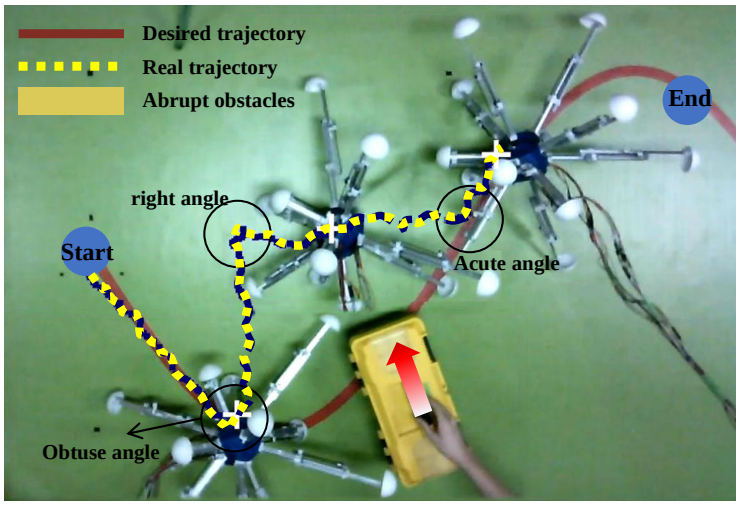

Fig. 9. Comprehensive performance demonstration experiment

4.2. Open-loop gait generation experiments

We performed an algorithm comparison test on the prototype to evaluate the proposed high-precision gait generation algorithm. The methods included in the comparison experiment included the open-loop manual discrete gait generation algorithm (Wagenknecht & Apostolopoulos, 2010) and inverse kinematics gait generation algorithm (Nozaki et al., 2018). The physics-driven gait planning method (Zhang et al., 2021) can also be employed as a gait generation algorithm but cannot be applied to a real robot and was thus excluded. We compared the error and standard deviation of the centroid trajectory in the open-loop gait deployment test of the prototype under three trajectories.

The experimental results are shown in Fig.10. We deployed the gait generated using the three methods in a straight line, an S-shaped trajectory, and an O-shaped trajectory. Each method was repeated five times under each scenario, and the mean and standard deviation were calculated. As shown in Fig.10-a, in all the experiments, the proposed method yielded the minimum error and maintained the minimum standard deviation, thus, demonstrating that the proposed method is highly accurate and stable.

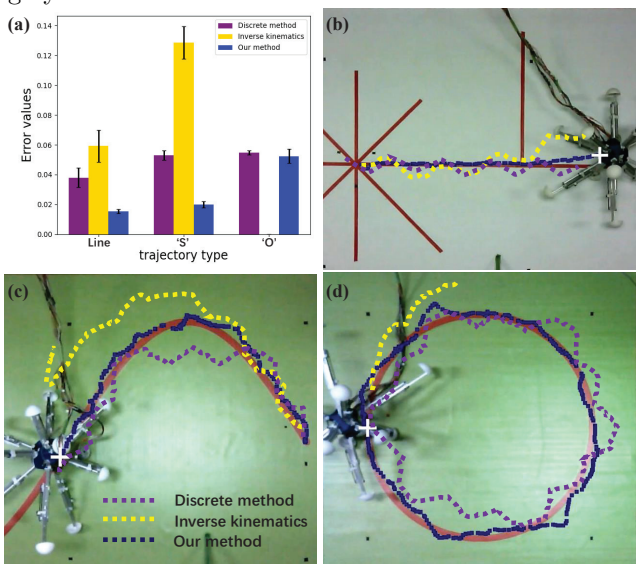

Fig. 10. Open-loop experiment error and three types of trajectory

In the straight-line experiment, all three methods completed the tracking task; however, the inverse kinematics method gradually deviated from the benchmark. The discrete gait presented a typical zigzag trajectory because it planned the gait based on the support triangle. The proposed method achieved a nearly linear trajectory. In the S-shaped trajectory, the actual trajectory of inverse kinematics method differed greatly from the desired trajectory. The tracking error of discrete gait was large when the radius of the circular track is very small. The proposed approach performed the best tracking. In the circular trajectory experiment, the inverse kinematics method tracked only a

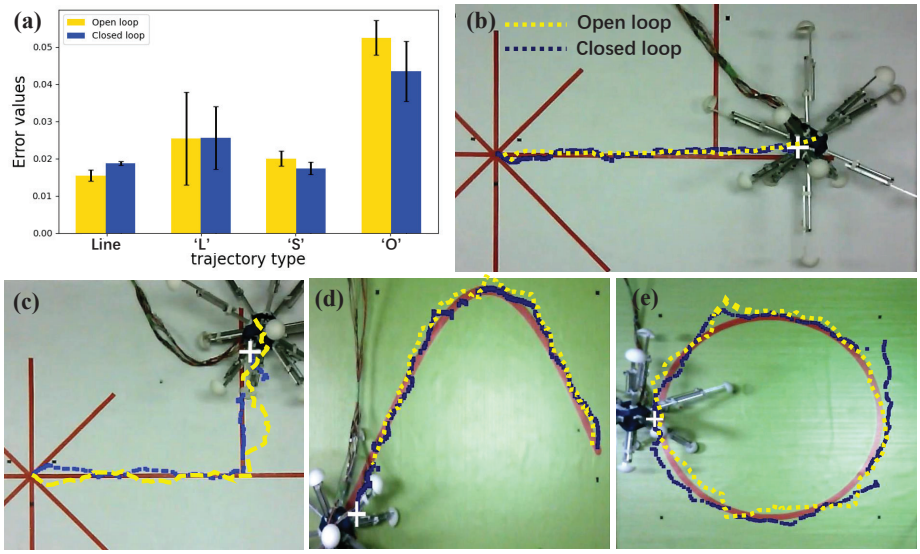

Fig. 11. Closed-loop trajectory tracking error

quarter of the circle; thus, the error could not be calculated. In contrast, the proposed method achieved the highest accuracy and stability. The prototype experiments demonstrated that the proposed simulation model could accurately predict the occurrence of sliding for planning high-precision open-loop gait in virtual environments.

4.3. Closed-loop gait control experiments

Our closed-loop control method is the first proposed motion control method for radial-skeleton robots. To verify the improved accuracy of the proposed compared with the formal open-loop gait deployment method, we performed the experiment on four types of trajectories, five times for each trajectory. To verify the robustness of the proposed motion control method, we conducted experiments in various interference environments and unseen obstacles.

Trajectory tracking accuracy test: We experimentally compared the closed-loop method with the open-loop gait generation method. The results are presented in Fig.11. In the straight-line trajectory experiment, the accuracy of the open-loop method was slightly higher than that of the closed-loop method. In other experiments, the accuracy of the closed-loop method was higher than that of the open-loop method. This demonstrates that in simple tracking tasks such as straight-line trajectory, the gait switching is smooth; thus, the proposed simulation model can achieve good simulation results and performance, even better than the closed-loop control. However, in complicated tracking tasks, errors are more likely to occur, and the closed-loop scheme can be replanned in real time to bridge the errors; thus, the accuracy of the open-loop method is lower than that of the closed-loop method.

Terrain robustness experiment: We performed two experiments to study the robustness, as seen in Fig.12. In the first experiment, to analyze the robustness against complex terrains, we constructed a complex obstacle terrain by using wooden boards with a maximum undulation of 50% of the robot's structural size. The robot could not perceive complex terrains and rely on the symmetrical multi-legged structure with no overturning and a high tolerance for terrain adaptation. The experiment was performed 20 times, and a success rate of 70% was achieved.

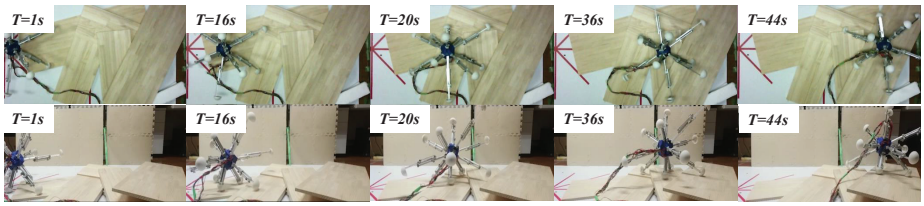

Fig. 12. Obstacle terrain adaptation experiments

External interference robustness experiment: In the second experiment, we manually intervened the robot on the predetermined linear motion to make it deviate from the trajectory, as shown in Fig.13. The experiment was performed 20 times; the robot recovered the originally established trajectories autonomously all 20 times.

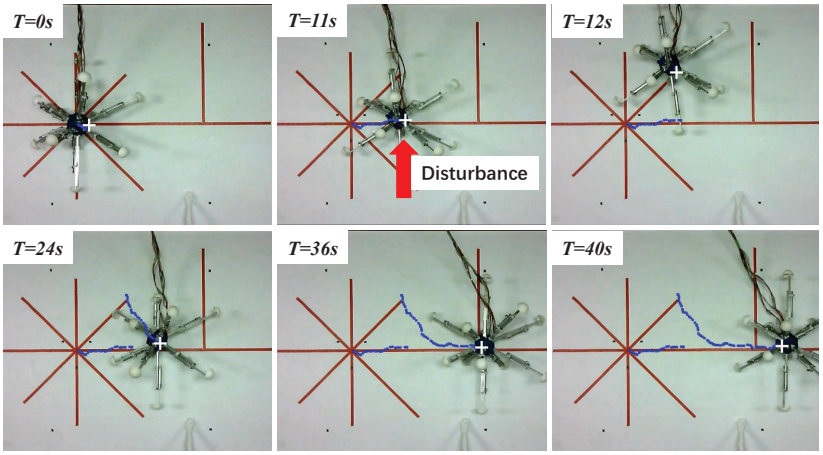

Fig. 13. External interference experiments

5. Conclusion

In this paper, we proposed a radial-skeleton robot comprising 12 telescopic legs. The proposed design with high elongation and symmetrical structure yield the advantages of omnidirectional motion and upright posture in complex terrains. In addition, we proposed a high-precision gait generation algorithm considering the friction contact dynamics model that is suitable for any multi-legged

radial-skeleton robot. Moreover, we proposed and implemented a closed-loop control algorithm for a radial-skeleton robot in simulation and prototype experiments to enable it to perform trajectory-tracking tasks with high accuracy, stability, and robustness. Finally, we compared the proposed method with existing methods to validate the proposed method. The results revealed that the proposed method offers advantages such as the capability to maneuver on unknown rugged surfaces and track trajectories with high accuracy.

However, there are limitations worthy of future research: more onboard sensors (force sensors, cameras, laser scanners, etc.) should be installed for independent planning without relying on external perception, and a control strategy based on a data-driven method must be established to achieve autonomous movement on complex terrains.

Acknowledgments

This work was supported by the National Natural Science Foundation of China [grant number 12022212].

References

Abourachid, A., Böhmer, C., Wenger, P., Chablat, D., Chevallereau, C., Fasquelle, B., & Furet, M. (2019). Modelling, design and control of a bird neck using tensegrity mechanisms. In *ICRA'2019 Worskhop on Tensegrity*. Doi: https://hal.archives-ouvertes.fr/hal-02355070.

Abrahantes, M., Silver, A., & Wendt, L. (2007). Gait design and modeling of a 12-tetrahedron walker robot. In *2007 Thirty-Ninth Southeastern Symposium on System Theory* (pp. 21–25). IEEE. Doi: https://doi.org/10.1109/SSST.2007.352310.

Antol, J. (2005). A new vehicle for planetary surface exploration-the mars tumbleweed rover. In *1st Space Exploration Conference: Continuing the Voyage of Discovery* (p. 2520).

Baines, R. L., Booth, J. W., & Kramer-Bottiglio, R. (2020). Rolling soft membrane-driven tensegrity robots. *IEEE Robotics and Automation Letters*, *5*, 6567–6574. Doi: https://doi.org/10.1109/LRA.2020.3015185.

Bicchi, A., Balluchi, A., Prattichizzo, D., & Gorelli, A. (1997). Introducing the" sphericle": an experimental testbed for research and teaching in nonholonomy. In *Proceedings of International Conference on Robotics and Automation* (pp. 2620–2625). IEEE volume 3. Doi: https://10.1109/ROBOT.1997.619356.

Bingyu, L., Ziyun, K., Haijun, P., Wenya, Z., & Zhigang, W. (2020). Design and research on a continuum manipulator based on tensegrity structure. *ROBOT*, *42*, 686–696. Doi: http://robot.sia.cn/CN/10.13973/j.cnki.robot.190642.

Crowe, C., Sommerfeld, M., Tsuji, Y. et al. (1998). *Multiphase Flow with Droplets and Particles*. Ž.

Dubowsky, S., Kesner, S., Plante, J.-S., & Boston, P. (2008). Hopping mobility concept for search and rescue robots. *Industrial Robot: An International Journal*, *35*, 238–245. Doi: https://10.1108/01439910810868561.

Gheorghe, V., Alexandrescu, N., Duminica, D., & Cartal, L. A. (2010). Rolling robot with radial extending legs. In *2010 3rd International Symposium on Resilient Control Systems* (pp. 107–112). IEEE. Doi: https://doi.org/10.1109/ISRCS.2010.5603951.

Hamlin, G. J., & Sanderson, A. C. (1994). A novel concentric multilink spherical joint with parallel robotics applications. In *Proceedings of the 1994 IEEE international conference on robotics and automation* (pp. 1267–1272). IEEE. Doi: https://doi.org/10.1109/ROBOT.1994.351313.

Hirano, T., Ishikawa, M., & Osuka, K. (2013). Control and development of cylindrical mobile robot. *Journal of Robotics and Mechatronics*, *25*, 392–399. Doi: https://10.20965/jrm.2013.p0392.

Hong, G. Y., & Choi, Y. (2019). Tensegrity wrist mechanism using three layers of rigid bodies and strings. In *2019 16th International Conference on Ubiquitous Robots (UR)* (pp. 728–733). IEEE. Doi: https://doi.org/10.1109/URAI.2019.8768647.

Hustig-Schultz, D., SunSpiral, V., & Teodorescu, M. (2017). Morphological optimization for tensegrity quadruped locomotion. In *2017 IEEE/RSJ International Conference on Intelligent Robots and Systems (IROS)* (pp. 3990–3995). IEEE. Doi: https://doi.org/10.1109/IROS.2017.8206253.

Joshi, V. A., Banavar, R. N., & Hippalgaonkar, R. (2010). Design and analysis of a spherical mobile robot. *Mechanism and Machine Theory*, *45*, 130–136. Doi: https://10.1016/j.mechmachtheory.2009.04.003.

Jung, E., Ly, V., Buderi, A., Appleton, E., & Teodorescu, M. (2019). Design and selection of muscle excitation patterns for modeling a lower extremity joint inspired tensegrity. In *2019 Third IEEE International Conference on Robotic Computing (IRC)* (pp. 282–287). IEEE. Doi: https://doi.org/10.1109/IRC.2019.00053.

Lee, J., Hwangbo, J., Wellhausen, L., Koltun, V., & Hutter, M. (2020). Learning quadrupedal locomotion over challenging terrain. *Science robotics*, *5*, eabc5986. Doi: https://10.1126/scirobotics.abc5986.

Lessard, S., Bruce, J., Jung, E., Teodorescu, M., SunSpiral, V., & Agogino, A. (2016). A lightweight, multi-axis compliant tensegrity joint. In *2016 IEEE International Conference on Robotics and Automation (ICRA)* (pp. 630–635). IEEE. Doi: https://doi.org/10.1109/ICRA.2016.7487187.

Li, Z., Cheng, X., Peng, X. B., Abbeel, P., Levine, S., Berseth, G., & Sreenath, K. (2021). Reinforcement learning for robust parameterized locomotion control of bipedal robots. In *2021 IEEE International Conference on Robotics and Automation (ICRA)* (pp. 2811–2817). IEEE. Doi: https://10.1109/ICRA48506.2021.9560769.

Liu, C.-H., Yao, Y.-A., Li, R.-M., Tian, Y.-B., Zhang, N., Ji, Y.-Y., & Kong, F.-Z. (2012). Rolling 4r linkages. *Mechanism and machine theory*, *48*, 1–14. Doi: https://doi.org/10.1109/ROBOT.1994.351134.

Luders, R. A., Apostolopoulos, D., & Wettergreen, D. (2008). Control strategies for a multi-legged hopping robot. In *2008 IEEE/RSJ International Conference on Intelligent Robots and Systems* (pp. 1519–1524). IEEE. Doi: https://doi.org/10.1109/IROS.2008.4651033.

Masuda, Y., & Ishikawa, M. (2017). Development of a deformation-driven rolling robot with a soft outer shell. In *2017 IEEE International Conference on Advanced Intelligent Mechatronics (AIM)* (pp. 1651–1656). IEEE. Doi: https://doi.org/10.1109/AIM.2017.8014255.

Mateos, L. A. (2020). Bionic sea urchin robot with foldable telescopic actuator. In *2020 IEEE/ASME International Conference on Advanced Intelligent Mechatronics (AIM)* (pp. 1063–1068). IEEE. Doi: https://doi.org/10.1109/AIM43001.2020.9158806.

Mintchev, S., Zappetti, D., Willemin, J., & Floreano, D. (2018). A soft robot for random exploration of terrestrial environments. In *2018 IEEE International Conference on Robotics and Automation (ICRA)* (pp. 7492–7497). IEEE. Doi: https://doi.org/10.1109/ICRA.2018.8460667.

Mirletz, B. T., Park, I.-W., Flemons, T. E., Agogino, A. K., Quinn, R. D., & SunSpiral, V. (2014). Design and control of modular spine-like tensegrity structures. In *World Conference of the International Association for Structural Control and Monitoring (IACSM)* ARC-E-DAA-TN15559. Doi: https://ntrs.nasa.gov/citations/20160005274.

Mojabi, P. et al. (2002). Introducing august: a novel strategy for an omnidirectional spherical rolling robot. In *Proceedings 2002 IEEE International Conference on Robotics and Automation (Cat. No. 02CH37292)* (pp. 3527–3533). IEEE volume 4. Doi: https://https://doi.org/10.1115/1.1789542.

Mukherjee, R., Minor, M. A., & Pukrushpan, J. T. (2002). Motion planning for a spherical mobile robot: Revisiting the classical ball-plate problem. *J. Dyn. Sys., Meas., Control*, *124*, 502–511.

Nozaki, H., Kujirai, Y., Niiyama, R., Kawahara, Y., Yonezawa, T., & Nakazawa, J. (2018). Continuous shape changing locomotion of 32-legged spherical robot. In *2018 IEEE/RSJ International Conference on Intelligent Robots and Systems (IROS)* (pp. 2721–2726). IEEE. Doi: https://doi.org/10.1109/IROS.2018.8593791.

Nozaki, H., Niiyama, R., Yonezawa, T., & Nakazawa, J. (2017). Shape changing locomotion by spiny multipedal robot. In *2017 IEEE International Conference on Robotics and Biomimetics (ROBIO)* (pp. 2162–2166). IEEE. Doi: https://doi.org/10.1109/ROBIO.2017.8324739.

Otani, T., Urakubo, T., Maekawa, S., Tamaki, H., & Tada, Y. (2006). Position and attitude control of a spherical rolling robot equipped with a gyro. In *9th IEEE International Workshop on Advanced Motion Control, 2006.* (pp. 416–421). IEEE. Doi: https://10.1109/AMC.2006.1631695.

Sastra, J., Chitta, S., & Yim, M. (2009). Dynamic rolling for a modular loop robot. *The International Journal of Robotics Research*, *28*, 758–773. Doi: https://doi.org/10.1177/0278364908099463.

Shah, D. S., Booth, J. W., Baines, R. L., Wang, K., Vespignani, M., Bekris, K., & Kramer-Bottiglio, R. (). Tensegrity robotics. *Soft Robotics*, . Doi: https://doi.org/10.1089/soro.2020.0170.

Shibata, M., & Hirai, S. (2010). Moving strategy of tensegrity robots with semiregular polyhedral body. In *Emerging Trends In Mobile Robotics* (pp. 359–366). World Scientific. Doi: https://doi.org/10.1142/97898143299270045.

Shintake, J., Zappetti, D., Peter, T., Ikemoto, Y., & Floreano, D. (2020). Bio-inspired tensegrity fish robot. In *2020 IEEE International Conference on Robotics and Automation (ICRA)* (pp. 2887–2892). IEEE. Doi: https://doi.org/10.1109/ICRA40945.2020.9196675.

Sugiyama, Y., & Hirai, S. (2006). Crawling and jumping by a deformable robot. *The International journal of robotics research*, *25*, 603–620. Doi: http://dx.doi.org/10.1109/IROS.2004.1389922.

Sun, J., Song, G., Chu, J., & Ren, L. (2019). An adaptive bioinspired foot mechanism based on tensegrity structures. *Soft Robotics*, *6*, 778–789. Doi: https://doi.org/10.1089/soro.2018.0168.

Takemori, T., Tanaka, M., & Matsuno, F. (2018). Gait design for a snake robot by connecting curve segments and experimental demonstration. *IEEE Transactions on Robotics*, *34*, 1384–1391. Doi: https://10.1109/TRO.2018.2830346.

Tilden, M. W. (1995). *Biomorphic robots as a persistent means for removing explosive mines*. Technical Report Los Alamos National Lab.(LANL), Los Alamos, NM (United States).

Vespignani, M., Friesen, J. M., SunSpiral, V., & Bruce, J. (2018). Design of superball v2, a compliant tensegrity robot for absorbing large impacts. In *2018 IEEE/RSJ International Conference on Intelligent Robots and Systems (IROS)* (pp. 2865–2871). IEEE. Doi: https://doi.org/10.1109/IROS.2018.8594374.

Wagenknecht, B., & Apostolopoulos, D. (2010). Locomotion strategies and mobility characterization of a spherical multi-legged robot. In *International Design Engineering Technical Conferences and Computers and Information in Engineering Conference* (pp. 1049–1058). volume 44106. Doi: https://doi.org/10.1115/DETC2010-28153.

Wait, K. W., Jackson, P. J., & Smoot, L. S. (2010). Self locomotion of a spherical rolling robot using a novel deformable pneumatic method. In *2010 IEEE International Conference on Robotics and Automation* (pp. 3757–3762). IEEE. Doi: https://10.1109/ROBOT.2010.5509314.

Wang, X., Ling, Z., Qiu, C., Song, Z., & Kang, R. (2022). A four-prism tensegrity robot using a rolling gait for locomotion. *Mechanism and Machine Theory*, *172*, 104828. Doi: https://doi.org/10.1016/j.mechmachtheory.2022.104828.

Wang, X., Wang, X., Zhang, Z., & Zhao, Y. (2016). Motion planning of kinematically redundant 12-tetrahedral rolling robot. *International Journal of Advanced Robotic Systems*, *13*, 23. Doi: https://doi.org/10.5772/62178.

Wei, X., Tian, Y., & Wen, S. (2019). Design and locomotion analysis of a novel modular rolling robot. *Mechanism and Machine Theory*, *133*, 23–43. Doi: https://doi.org/10.1016/j.mechmachtheory.2018.11.004.

Wilson, J. L., Mazzoleni, A. P., DeJarnette, F. R., Antol, J., Hajos, G. A., & Strickland, C. V. (2008). Design, analysis and testing of mars tumbleweed rover concepts. *Journal of spacecraft and rockets*, *45*, 370–382. Doi: https://doi.org/10.2514/1.31288.

Xian, G., & Yongchun, F. (2020). Locomotion gait control for bionic robots: A review of reinforcement learning methods. *CAAI transactions on intelligent systems*, *15*, 152–159. Doi: https://10.11992/tis.201907052.

Yamawaki, T., Mori, O., & Omata, T. (2003). Nonholonomic dynamic rolling control of reconfigurable 5r closed kinematic chain robot with passive joints. In *2003 IEEE International Conference on Robotics and Automation (Cat. No. 03CH37422)* (pp. 4054–4059). IEEE volume 3. Doi: https://doi.org/10.1109/ROBOT.2003.1242220.

Yang, C., Yuan, K., Zhu, Q., Yu, W., & Li, Z. (2020). Multi-expert learning of adaptive legged locomotion. *Science Robotics*, *5*, eabb2174. Doi: https://10.1126/scirobotics.abb2174.

Yang, D., Yang, S., Yu, Y., & Wang, Q. (2022). Design and experiment of complex terrain adaptive robot based on deep re-inforcement learning. *Journal of Astronautics*, *43*, 1176–1185. Doi: https://10.3873/j.issn.1000-1328.2022.09.005.

Yim, M. (1994). New locomotion gaits. In *Proceedings of the 1994 IEEE International conference on Robotics and Automation* (pp. 2508–2514). IEEE. Doi: https://doi.org/10.1109/ROBOT.1994.351134.

Yim, M., Duff, D. G., & Roufas, K. D. (2000). Polybot: a modular reconfigurable robot. In *Proceedings 2000 ICRA. Millennium Conference. IEEE International Conference on Robotics and Automation. Symposia Proceedings (Cat. No. 00CH37065)* (pp. 514–520). IEEE volume 1. Doi: https://doi.org/10.1109/ROBOT.2000.844106.

Zagal, J. C., Armstrong, C., & Li, S. (2012). Deformable octahedron burrowing robot. In *ALIFE 2012: The Thirteenth International Conference on the Synthesis and Simulation of Living Systems* (pp. 431–438). MIT Press. Doi: http://dx.doi.org/10.7551/978-0-262-31050-5-ch057.

Zhang, F., Yu, Y., Wang, Q., & Zeng, X. (2021). Physics-driven locomotion planning method for a planar closed-loop terrain-adaptive robot. *Mechanism and Machine Theory*, *162*, 104353. Doi: https://10.1016/j.mechmachtheory.2021.104353.